Evaluating carbon dots as electron mediators in photochemical and photocatalytic processes of NiFe$_2$O$_4$

Lucy M. Ombaka [iD], Ralf Dillert, Lars Robben, and Detlef W. Bahnemann

COLLECTIONS

Paper published as part of the special topic on Solar to Fuel
Note: This paper is part of the Special Issue on Solar to Fuel.

View Online   Export Citation   CrossMark

ARTICLES YOU MAY BE INTERESTED IN

Current loss analysis in photoelectrochemical devices
APL Materials **8**, 031107 (2020); https://doi.org/10.1063/1.5142561

Antiferromagnetic and dielectric behavior in polycrystalline GdFe$_{0.5}$Cr$_{0.5}$O$_3$ thin film
APL Materials **8**, 031106 (2020); https://doi.org/10.1063/1.5142177

Spray-processed nanoporous BiVO$_4$ photoanodes with high charge separation efficiency for oxygen evolution
APL Materials **8**, 031112 (2020); https://doi.org/10.1063/1.5144107

8, 031105

Evaluating carbon dots as electron mediators in photochemical and photocatalytic processes of NiFe₂O₄

View Online   Export Citation   CrossMark

Lucy M. Ombaka,[1,2,a)]   Ralf Dillert,[1,3]   Lars Robben,[4]   and   Detlef W. Bahnemann[1,3,5,a)]

AFFILIATIONS

[1]Gottfried Wilhelm Leibniz Universität Hannover, Institut für Technische Chemie, Callinstrasse 3, Hannover D-30167, Germany

[2]School of Chemistry and Material Science, Technical University of Kenya, P.O. Box 52428-00200, Nairobi, Kenya

[3]Gottfried Wilhelm Leibniz Universität Hannover, Laboratorium für Nano- und Quantenengineering, Schneiderberg 39, Hannover 30167, Germany

[4]FB2, Institute of Inorganic Chemistry and Crystallography, University of Bremen, Leobener Strasse 7, D-28359 Bremen, Germany

[5]Laboratory for Photoactive Nanocomposite Materials, Department of Photonics, Faculty of Physics, Saint-Petersburg State University, Ulianovskaia Str. 3, Peterhof, Saint-Petersburg 198504, Russia

Note: This paper is part of the Special Issue on Solar to Fuel.
[a)]Authors to whom correspondence should be addressed: lucyombaka@gmail.com and bahnemann@iftc.uni-hannover.de

ABSTRACT

Spinel ferrites such as nickel ferrite are promising energy conversion photocatalysts as they are visible-light absorbers, chemically stable, earth abundant, and inexpensive. Nickel ferrite shows poor photocatalytic activity due to fast electron–hole recombination upon illumination. This study evaluates the capability of carbon dots (CDs) to improve charge-carrier separation in NiFe₂O₄. We report a facile solvothermal approach for synthesizing NiFe₂O₄ and CDs/NiFe₂O₄ nanoparticles at 200–215 °C. The photocatalysts were characterized using transmission and scanning electron microscopy, x-ray diffraction, Raman spectroscopy, Fourier transform infrared spectroscopy, UV-VIS-NIR spectroscopy, photoelectrochemical analysis, and laser flash photolysis. Photocatalytic oxidation of methanol to formaldehyde under visible light was employed to test the effect of CDs on the photocatalytic efficacy of NiFe₂O₄. UV-VIS-NIR spectroscopy depicted a total quenching of NIR absorption and a diminished absorption of a peak at ~745 nm in CDs/NiFe₂O₄ compared with NiFe₂O₄, indicating a transfer of electrons from NiFe₂O₄ to CDs. A 12-fold increment in the incident-photon-to-charge-efficiency was achievable with CDs/NiFe₂O₄ (0.36%) compared with NiFe₂O₄ (0.03%). Impedance spectroscopy exhibited a more efficient charge separation and faster interfacial charge transfer in CDs/NiFe₂O₄ compared with pure NiFe₂O₄. This was accounted for by the lower initial quantity of charge carrier upon irradiation in CDs/NiFe₂O₄ compared with NiFe₂O₄ as detected from laser flash photolysis, indicating that CDs acted as electron acceptors and reservoirs in CDs/NiFe₂O₄. Compared with NiFe₂O₄, CDs/NiFe₂O₄ showed an enhanced photocatalytic activity toward formaldehyde formation. Consequently, CDs are good electron mediators for NiFe₂O₄, capable of improving charge-carrier separation and the photocatalytic activity of NiFe₂O₄.

INTRODUCTION

The feasibility of actualizing a sustainable environment heavily relying on photocatalytic conversion of renewable resources to fuel is largely hampered by the unavailability of highly efficient and inexpensive photocatalysts.[1,2] At present, numerous research projects focus on the development of inexpensive, efficient, and chemically stable photocatalysts, capable of converting renewable resources such as sunlight, water, and biomass to fuel.[3,4] Such an approach toward obtaining green energy is deemed smart

and sustainable. Despite the great emphasis laid on utilizing renewable resources for fuel production, to date non-renewable resources such as fossil deposits remain the major source of consumer fuel. This is partly due to the aforementioned challenges, thus necessitating a continuous improvement of the existing photocatalytic systems or the development of new efficient and inexpensive photocatalysts. One promising approach toward engineering a low-cost, efficient, and chemically stable photocatalyst is enhancing the photochemical properties of inorganic semiconductors exhibiting visible-light absorption.[2]

Spinel ferrites, which are mixed oxides of iron and a single or numerous metals, are one such example of visible-light absorbing inorganic semiconductors widely studied for their photocatalytic activity.[5,6] This is due to their attractive photochemical properties such as narrow optical bandgaps (<2 eV),[7] good photochemical stability,[6,8] natural abundance that lowers their cost of purchase, ease of optoelectronic modification,[9] and facile cost-effective synthetic procedures.[5] Spinel ferrites have the general formula $M^{2+}Fe_2^{3+}X_4^{2-}$, where M^{2+} is a bivalent metallic cation and X_4^{2-} is a chalcogenide such as an oxide.[10] Some spinel ferrites show good magnetic properties while others do not.[10,11] Spinel ferrites crystallize into cubic structures in which the anion X_4^{2-} arranges itself into a close-packed cubic structure, while the cations M^{2+} and Fe_2^{3+} occupy the tetrahedral (T) and octahedral (O) sites in varying quantities.[7,12] This variation in the ratios of cations occupying the latter to the former sites is called the degree of inversion. The degree of inversion is low for normal spinel ferrites (e.g., zinc ferrite) and high for inverse spinel ferrites such as nickel ferrite which is a well-known ferromagnetic semiconductor.[13,14] When used as a photocatalyst or a co-catalyst, the ferromagnetic nature of nickel ferrite enables its convenient recovery from a reaction solution by using a magnet, which is an added advantage. Despite the reported good physical and photochemical properties of spinel ferrites, most of them, including nickel ferrite, exhibit lower photocatalytic activities than expected owing to bulk charge-carrier recombination and Fermi level pinning.[9] Thus, the exploration of various techniques for the improvement of charge-carrier separation in nickel ferrites is a worthwhile venture. Among various applicable techniques, an interesting approach of enhancing the charge-carrier separation in nickel ferrite is to chemically coordinate it to stable and inexpensive electron mediators such as carbon dots (CDs).[15]

Discovered in 2004, CDs that consist of a carbon core and various surface chromophores are the latest known subclass of carbon nanomaterials.[16] Most CDs are spherical in nature and exhibit good fluorescence efficiency.[17] As the most recent carbon nanomaterials, CDs have intrigued the research community due to their unique properties, including simple synthetic techniques from inexpensive precursors,[4,18] biocompatibility and aqueous dispersibility,[18] ease of functionalization,[19] outstanding chemical and photo-stability,[20] and a large electron-storage capacity.[19] Some reports propagate CDs as good electron–hole separators in a CDs/semiconductor composite. This may be attributed to their capacity to act as charge reservoirs.[4] However, limited accounts report an in-depth experimental study on exactly how and if CDs influence the photocatalytic properties of spinel ferrites.[21] This account aimed at experimentally analyzing the ability of CDs to improve charge separation in nickel ferrite. Nickel ferrite and CDs/nickel ferrite nanoparticles were synthesized and

characterized. The emphasis was laid on determining the difference between the physicochemical, optical, photochemical, and photocatalytic properties of the two materials. Particular attention was paid to the influence of CDs on charge-carrier properties of nickel ferrite; this was inferred from electrochemical analysis and laser flash photolysis.

EXPERIMENTAL

All reagents and solvents used were of analytical grade and hence used as received from the supplier. Nickel(II) acetylacetonate [Ni(acac)₂ 98.0%], iron(III) acetylacetonate [Fe(acac)₃ 99.0%], citric acid (≥99.5%), ethylenediaminetetraacetic acid (99%), triethylene glycol (99%), potassium hydroxide (KOH 99.0%), methanol (99.8%), and tetraethylenepentamine were purchased from Merck, Germany. The catalysts were synthesized in a 50 ml Pyrex test tube fitted with a Schott GL25 threaded cap containing a rubber septum.

Nickel ferrite was synthesized via a solvothermal approach designed by modifying the method reported by Wang *et al.*[22] In a typical synthetic procedure, 0.7 mmol (181.1 mg) of Ni(acac)₂ and 1.4 mmol (493.9 mg) of Fe(acac)₃ were mixed in a sealable pressure tube and suspended in 14 ml of triethylene glycol at room temperature. The reaction tube was then sealed and the suspension heated to 200 °C and maintained at this temperature for a period of 2 h. Within the first 15 min of heating, the suspension was hand-shaken at intervals of 5 min, resulting in the formation of a dark solution. After the 2 h reaction period, the reactor tube was cooled to room temperature. Thereafter, 10 ml of the dark solution was mixed with 40 ml of ethyl acetate, and then centrifuged at 2000 rpm for 5 min to obtain a black supernatant and a black precipitate. The black supernatant was discarded leaving behind a black solid, which was washed 3 times with 3-aliquots of 40 ml ethyl acetate and agitated by hand shaking. For each wash, the solid was reclaimed by centrifuging the mixture at 2000 rpm for 5 min followed by discarding the supernatant. The obtained clean black solid was oven dried for 12 h at 70 °C then pulverized using a clean pestle and mortar, and finally calcined at 400 °C in oxygen for 12 h to yield a dark-brown powder of nickel ferrite that was labeled NFO.

The CDs/nickel ferrite composite was prepared by *in situ* solvothermal deposition of carbon dots onto the surface of pre-synthesized NFO. The procedure utilized was based on modifications of the protocol reported by Wang *et al.*[23] In brief, the composite was formed by mixing 100 mg NFO, 500 mg of citric acid, and 500 mg ethylenediaminetetraacetic acid in a sealable pressure tube and suspending the mixture in 14 ml of tetraethylenepentamine at room temperature.[24] The reactor tube was then sealed and heated to 215 °C with constant hand shaking at 5 min intervals within the first 15 min of heating, to obtain a near homogeneous suspension. This reaction temperature was maintained for a period of 7 h after which, the reaction was left to cool to room temperature. A yellow-brown supernatant with residual black depositions at the base of the reaction tube was obtained. The supernatant was decanted, and then the black residue washed with 40 ml of ethanol and agitated by hand shaking. This was followed by centrifugation at 2000 rpm for 5 min after which, the subsequent supernatant was discarded and the wash repeated three times. The obtained solid was washed with 40 ml of water, agitated by hand shaking, centrifuged at 2000 rpm for 5 min then the clear supernatant discarded

leaving behind a solid. The resulting solid was then oven dried for 12 h at 70 °C to yield the CDs/nickel ferrite composite, which was labeled NFO–C.

Electron micrographs of both samples were acquired using transmission electron microscopy (TEM) and scanning electron microscopy (SEM). TEM was conducted on a FEI Tecnai G2 F20 TMP fitted with a 200 kV field emission gun, while SEM was conducted on a JEOL JSM-6700F equipped with a lower secondary electron image detector. The nanoparticle size of the samples was determined by measuring the diameters of at least 50 nanoparticles sampled from the TEM micrographs of each sample. X-ray diffraction (XRD) patterns were collected on a StadiMP diffractometer (Stoe & Cie., Darmstadt, Germany) using monochromatized $Mo_{K\alpha}$ radiation (λ = 70.93 pm), Debye–Scherrer geometry (0.3 mm glass capillary), and approximately 10 wt. % silicon powder as internal standard. Rietveld refinements were carried out using Topas V.6 (Bruker AXS). Profile functions were calculated based on the first principles method included in the program and LaB_6 as a standard material. Structure refinements were set up using structure models for Trevorite (ICSD 28108) and Silicon (ICSD 652258); additional single peaks were used to include amorphous scattering contributions from the capillary.

Functional groups present in both samples were evaluated using an attenuated total reflection Fourier transform infrared spectroscopy (ATR-FTIR) (Bruker IFS66v spectrometer of spectral range 50–10 000 cm^{-1}). Isotopic composition of stable C (^{13}C and ^{12}C) and N (^{15}N and ^{14}N) isotopes as well as the quantitative composition of C and N in the ground plant material was measured on an elemental analyzer (Isotope Cube, Elementar, Hanau—Germany) coupled with an isotopic ratio mass spectrometer (Isoprime 100, Isoprime, Manchester—Great Britain). Raman spectroscopy was conducted at an incident laser beam of 633 nm by use of a confocal Bruker Senterra micro-Raman spectrometer. Dynamic light scattering particle size analysis and zeta potential measurements were conducted on a particle analyzer (Anton Paar Litesizer^{TM} 500) in double distilled water at 20 °C. Optical properties of catalysts were evaluated by using UV-VIS-NIR spectrometer (Agilent Carry 5000 fitted with an external DRA-2500 Diffuse Reflectance Accessory).

Incident-photon-to-current efficiency (IPCE) and electrochemical impedance spectroscopy (EIS) were evaluated on a Zennium potentiostat connected to a PECC-2 photoelectrochemical cell (Zahner-Elektrik GmbH & Co. KG). The cell consisted of a Teflon vessel containing a KOH (1M) electrolyte, a Pt counter electrode, a Ag/AgCl/KCl (3M) reference electrode, and a working electrode. The working electrode was prepared via the doctor blade method by coating a paste comprising the catalyst (200 mg), Triton X-100 (100 ml), polyethylene glycol 1000 (Merck) (100 mg), and deionized water (400 ml) onto the conductive side of fluorine-doped tin oxide (FTO) films (Sigma-Aldrich). The coated films were then calcined in air at 500 °C for 2 h prior to usage as the working electrode. Time resolved transient reflectance spectroscopy was conducted at an excitation wavelength of 355 nm, an energy of 1.5 mJ, and a resistance of 1000 Ω, as previously reported.[25] The spectra were recorded using a laser flash spectrometer [Nd-YAG laser (Brilliant B, Quantel)] equipped with a laser flash photolysis spectrometer (LKS 80, Applied Photophysics) and an optical parametric oscillator (OPO) (MagicPRISM, OPOTEK, Inc.).

Photocatalytic performance of both catalysts and CDs toward oxidation of methanol to formaldehyde was conducted in oxygen at atmospheric temperature and pressure. For the photocatalytic tests, 60 mg of the catalyst was weighed into a transparent glass container (95 cm^2) and suspended in 30 ml solution containing 10% v/v MeOH. The mixture was stirred at 500 rpm and left for 30 min to equilibrate in a dark room. Afterward, the suspension was illuminated with visible light (λ < 450 nm or 660 nm) for a period of 2 h. A LED lamp (450 W, Mueller Elektronik-Optik) with an irradiance of 72 W/m^2 was used to emit the 450 nm wavelength, while the 660 nm wavelength was emitted by a monochromatic LED light source (Thorlabs) with an irradiance of 0.59 W/m^2. The reaction progress was monitored at 30 min intervals by taking 300 μl aliquots, which were mixed with 300 μl Nash reagent (a solution of 15 g ammonium acetate, 0.2 ml acetylacetonate, and 0.3 ml acetic acid in 100 ml of Millipore water) and left to react overnight.[26] Afterward, the quantity of formaldehyde was analyzed by using UV-VIS spectrometry (Agilent).

RESULTS AND DISCUSSION

Synthesis of NFO and NFO–C

Solvothermal synthesis of nickel ferrite at 200 °C using triethylene glycol as a surfactant yielded NFO as a dark reddishbrown powder. The coordination of CDs to NFO was achieved via a novel procedure that employed ethylenediaminetetraacetic acid, tetraethylenepentamine, and citric acid as multiple centers for primary and secondary amine acylation with carboxylic acid (Scheme 1).[27]

Three distinct phases marked the formation of CDs in the presence of NFO. At the reaction onset, ethylenediaminetetraacetic acid and citric acid dissolved in tetraethylenepentamine at a temperature of 215 °C to form a clear supernatant above NFO that settled as a residue at the base of the reaction tube. During this first phase, it is possible that the amines in tetraethylenepentamine react with the carbonyl groups in citric acid and ethylenediaminetetraacetic acid forming polycyclic aromatics (Scheme 1).[18] After 15 min of reaction, the clear supernatant turns into a black-brown solution. This stage is associated with the carbonization of the polycyclic aromatic rings to form CDs leaving nitrogen and oxygen moieties in the supernatant.[28] A further heating of the reactants for a period of 15 min turns the dark-brown supernatant into a brighter yellow-brown solution. This phase is associated with surface passivation of the CDs with nitrogen and oxygen moieties that alters the optical properties of CDs. Continued heating of the suspension of functionalized CDs and NFO under the developed pressure results in coordination of the CDs to NFO.

Morphological analysis

The structural and morphological properties of NFO and NFO–C were evaluated by using TEM and SEM (Figs. 1 and 2). Micrographs of CDs present in the reactions' supernatant depict the CDs as elongated and fused spheres [Figs. 1(a) and 1(b)]. TEM images of NFO and NFO–C exhibit the formation of irregularly shaped spheres similar to those shown in other reports.[29,30] Both samples were crystalline with visible lattice fringes of 0.25 nm,
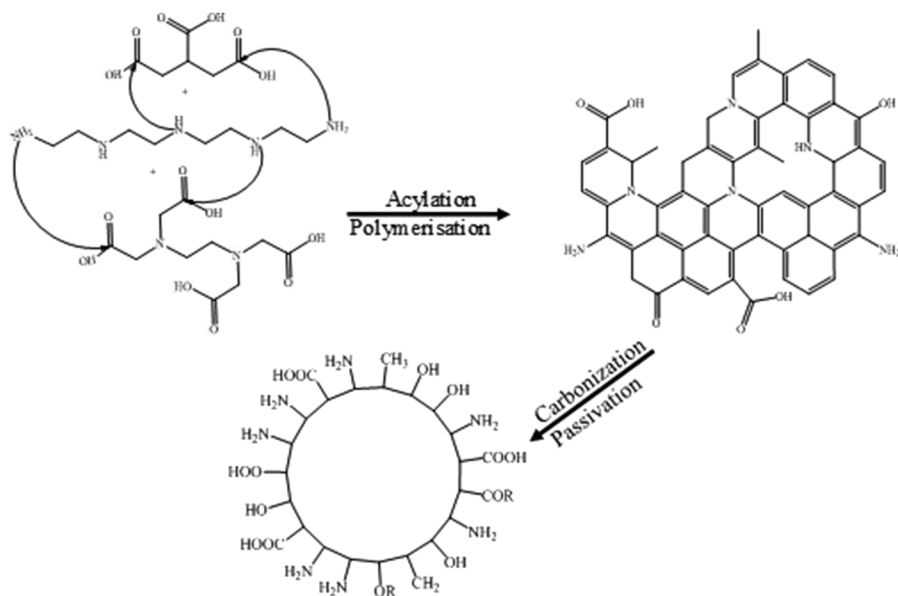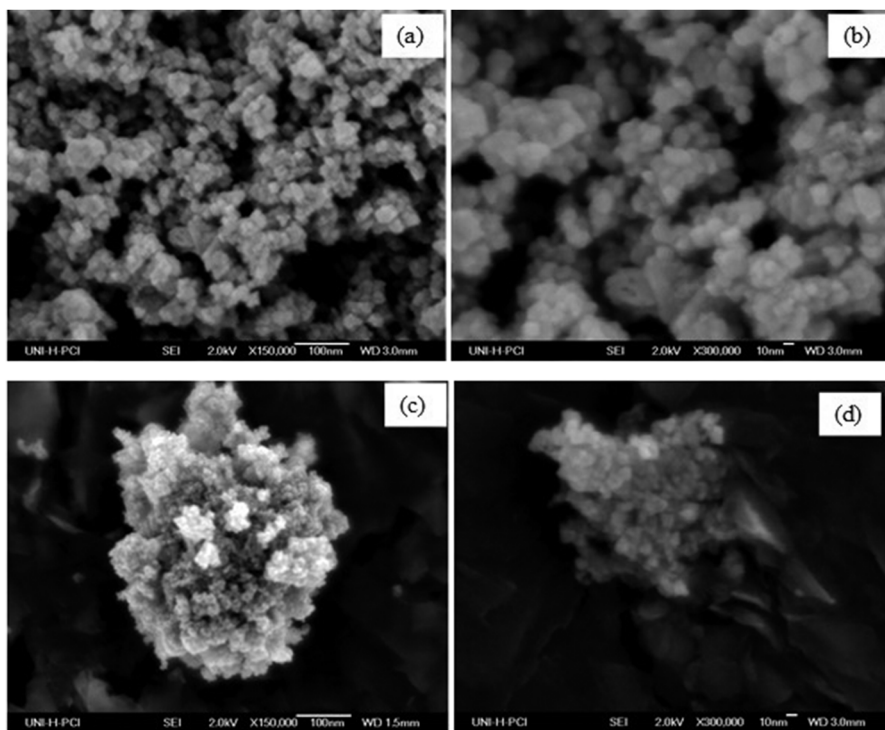
SCHEME 1. Schematic representation of the solvothermal synthesis of CDs.
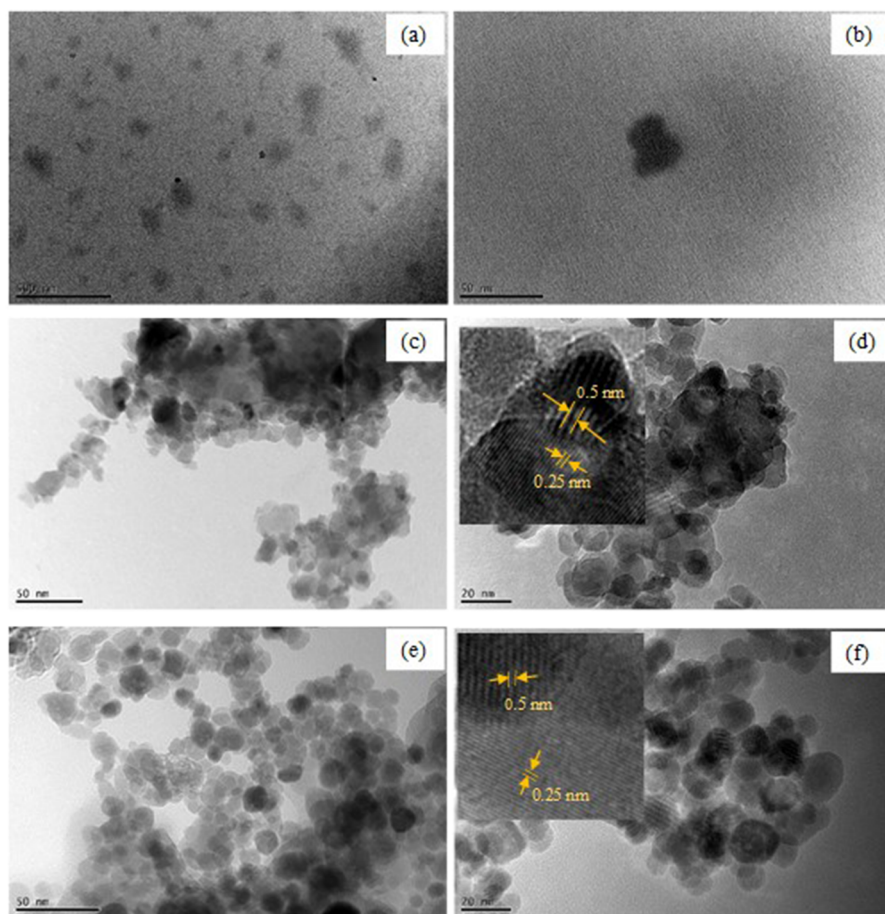
FIG. 1. TEM micrographs of CDs at lower (a) and higher (b) magnification, NFO at lower (c) and higher (d) magnification, and NFO–C at lower (f) and higher (g) magnification.

FIG. 2. SEM micrographs of NFO at a lower (a) and higher (b) magnification and NFO–C at lower (c) and higher (d) magnification.

0.29 nm, and 0.51 nm corresponding to the (311), (220), and (111) planes of NFO [Figs. 1(c) and 1(d)].[31] This implies that the conjugation of CDs to NFO did not alter the crystallinity of NFO. Particle size analysis of the TEM micrographs gave a diameter of 11.1 nm and 11.3 nm for NFO and NFO–C, respectively. Thus, the conjugation of CDs to NFO did not alter the particle size of NFO. Carbon nanoparticles are not observable in the TEM micrographs of NFO–C [Figs. 1(e) and 1(f)]. However, a lattice fringe of 0.31 nm was measured in NFO–C. This may indicate that the CDs form a thin carbon coating over NFO nanoparticles. DLS analysis of the CDs present in the reactions' supernatant exhibited four categories of CDs with diameters in the range of 0.7–0.8 nm, 1.7 nm, 1216.0–1976.9 nm, and 9989.0–19 095.4 nm (see the supplementary material, S1). Since, the TEM micrographs of NFO–C did not depict particles larger than 500 nm; it is probable that the larger carbon particles (>500 nm) observed from the DLS graph of CDs did not conjugate to NFO. Instead, these particles were washed off from the catalyst surface during the purification procedure.

SEM micrographs of NFO and NFO–C depict the formation of fused spheres (Fig. 2). The spheres in the SEM images of NFO–C appear to have a slightly better dispersion and interaction with the graphite sample holder than NFO. The improved dispersion can be associated with functionalization of NFO with CDs having N and O functional groups. The presence of such functional groups grafted onto the surface of NFO–C was further probed by zeta potential analysis. NFO showed a potential of −7.0 mV and a conductivity of 0.05 mS/cm, while NFO–C showed a potential of −18.4 mV and conductivity of 0.11 mS/cm. The increased zeta potential and

conductivity in NFO–C are associated with the presence of surface functional groups such as carboxylic and amine groups, which have been reported to be present in nitrogen-doped CDs.[17]

X-ray diffraction

The results of the Rietveld refinements of the XRD diffractograms of NFO and NFO–C are presented in Figs. 3(a) and 3(b), respectively. Both datasets can be refined to very good R_{wp} values using only the Trevorite crystal structure (ICSD 28108) and the internal standard (for details, see the supplementary material, S2).[32] Consequently, it is apparent that both samples crystallized in the face centered cubic inverse spinel structure.[29] Reflections from hexagonal graphite or amorphous carbon were not noticeable in the observed diffractograms of both samples.[33] The average crystallite size L_{volIB} of NFO and NFO–C was 18(2) nm and 19(1) nm, respectively.

Raman spectroscopic analysis

Raman spectroscopy was used to determine phase purity and cationic distribution in tetrahedral (T) and octahedral (O) sites in the nickel ferrites (NFOs). NFOs are inverse spinels [space group $Fd\bar{3}m$, (O_h^7)], implying that $\frac{1}{2}$ Fe^{3+} ions occupy all the T-sites, while the remaining $\frac{1}{2}$ Fe^{3+} and Ni^{2+} ions occupy the O-sites.[34] The Raman spectra of NFO and NFO–C (Fig. 4 and Table I) exhibit five active Raman internal modes characteristic of nickel ferrites.[34] From the presented spectra, no phase impurity such as hematite was observed.[7] Table I summarizes the peak maxima and their full
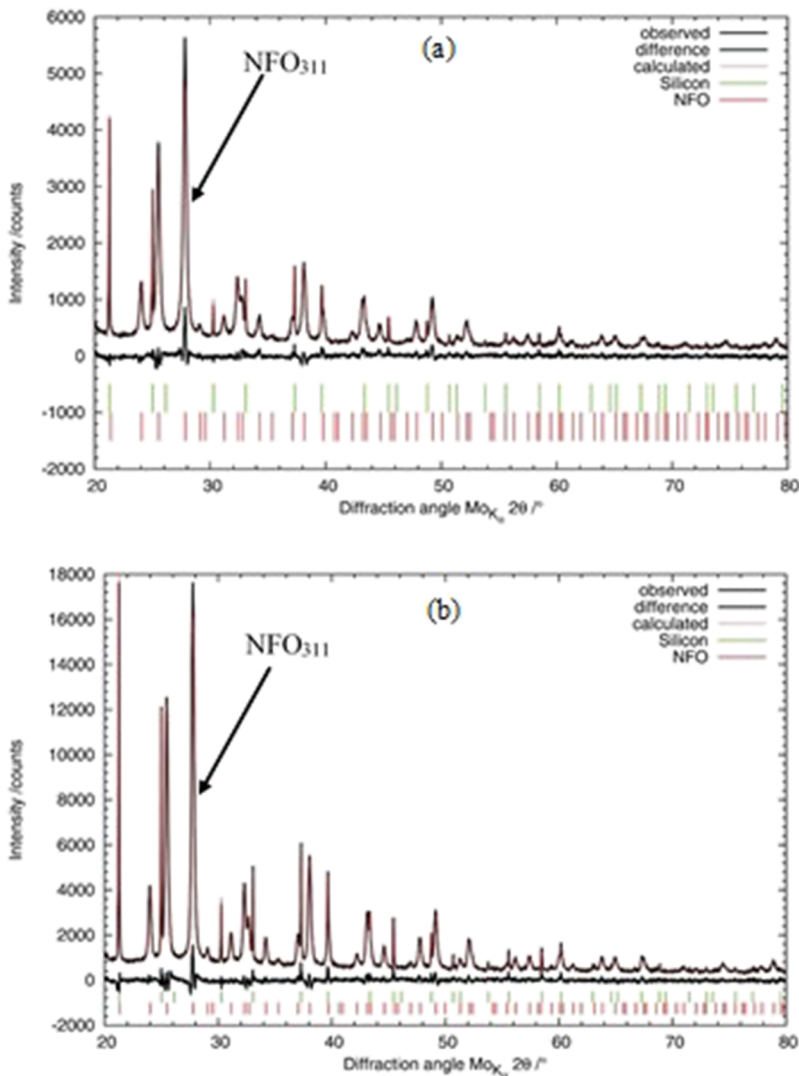
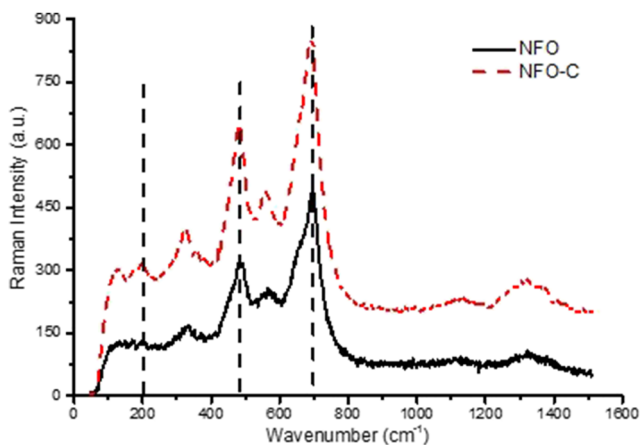**FIG. 3**. XRD diffractograms of NFO (a) and NFO–C (b).

FIG. 4. Raman spectra of NFO and NFO–C.

width at half maxima (FWHM) as observed from the Raman spectra of NFO and NFO–C. The main peaks can broadly be categorized into vibrational modes of octahedral groups (490–610 cm^{-1}) and tetrahedral groups (610–760 cm^{-1}).[35] A peak at 193 cm^{-1} was present in the spectra of NFO–C but absent in the spectra of NFO. This peak possibly arises from the radial breathing mode (RBM) of single or double walled nitrogen-doped carbon sheets conjugated to nickel ferrite.[36] The predominance of this peak in NFO–C compared with NFO is evidence of the successful conjugation of CDs to NFO.

The peaks positioned in the range 600–800 cm^{-1} consist of overlapping peaks that exhibit a broad shoulder toward lower wavelengths. This shoulder at ~670 cm^{-1} appears diminished in NFO–C compared with NFO. A least-squares fitting using Gaussian functions gave two distinct peaks (Table I) characteristic of NFOs.[31] A comparison of the FWHM of the main peaks in the O-site (568 cm^{-1} and 558 cm^{-1} in NFO and NFO–C, respectively) and T-site (697 cm^{-1} and 693 cm^{-1} in NFO and NFO–C, respectively)

TABLE I. Raman vibrational modes and FWHM of NFO and NFO–C.

Raman vibration mode	NFO		NFO–C	
	Frequency (cm^{-1})	FWHM (cm^{-1})	Frequency (cm^{-1})	FWHM (cm^{-1})
T_{2g}	. . .	. . .	193	57
E_g	330	37	326	34
T_{2g}	482	57	480	56
A_{1g}	568	62	558	34
E_g	669[a]	117	671[a]	112
A_{1g}	697	31	693	37

[a]Implies a peak shoulder.

reveals that the FWHM of the O-site peak in NFO–C is lesser, while that of the T-site is greater than their corresponding peaks in NFO. This phenomenon is indicative of the migration of Fe^{3+} ions from the O-site to the T-site of NFO, resulting in an increased degree of inversion upon functionalization of NFO with CDs.[35] Thus, it is plausible that the conjugation or post-treatment of NFO with CDs increases the degree of inversion in NFO–C. It is interesting to note that the peak at 326 cm^{-1} in NFO–C exhibits a broad shoulder, while its corresponding peak in NFO at 330 cm^{-1} does not. This could be due to the increased degree of inversion as was reported for the case of zinc ferrites having increased degrees of inversion.[7] However, further studies are required to verify this claim. In overall, we noted that the coordination of CDs to NFO could have resulted in an increased number of defects in the spinel, which in turn increases the degree of inversion that can affect both conductivity and photocatalytic properties of NFO.

Elemental and FTIR analysis

The amount of carbon and nitrogen present in NFO and NFO–C was quantified by using an elemental analyzer and the obtained elemental compositions summarized in Table II. Pristine NFO contained lower quantities of carbon and nitrogen (0.01 and 0.09, respectively) compared to NFO–C (0.18 and 0.51, respectively). The increase in C and N content in NFO–C is attributable to the presence of nitrogen-containing CDs in this sample, hence indicating that CDs were successfully conjugated to NFO via the solvothermal approach.

FTIR was used to qualitatively analyze the functional groups present in NFO and NFO–C. The metal–oxygen vibrational modes at the tetrahedral and octahedral sites of ferrites are reported to predominantly occur between 650 cm^{-1}–500 cm^{-1} and 450–358 cm^{-1}, respectively.[37–39] From the FTIR spectra [Fig. 5(a)], both samples exhibit two distinct peaks at 775 cm^{-1} and 445 cm^{-1} ascribed to

M^{x+}–O vibrations at the tetrahedral and octahedral sites, respectively.[11] The observed peak frequencies associated with tetrahedral site vibrations in NFO and NFO–C were higher than those reported in previous accounts.[38,40] This shift in frequencies can be attributed to structural differences in NFOs arising from different surfactants used during synthesis. A shift of ≈21 cm^{-1} toward higher frequencies is noticeable in the 775 cm^{-1} peak of NFO–C compared with

TABLE II. A summary of the quantitative C and N compositions in NFO and NFO–C.

Catalyst	C (%)	N (%)	C/N
NFO	0.01	0.09	8.9
NFO–C	0.18	0.51	2.8
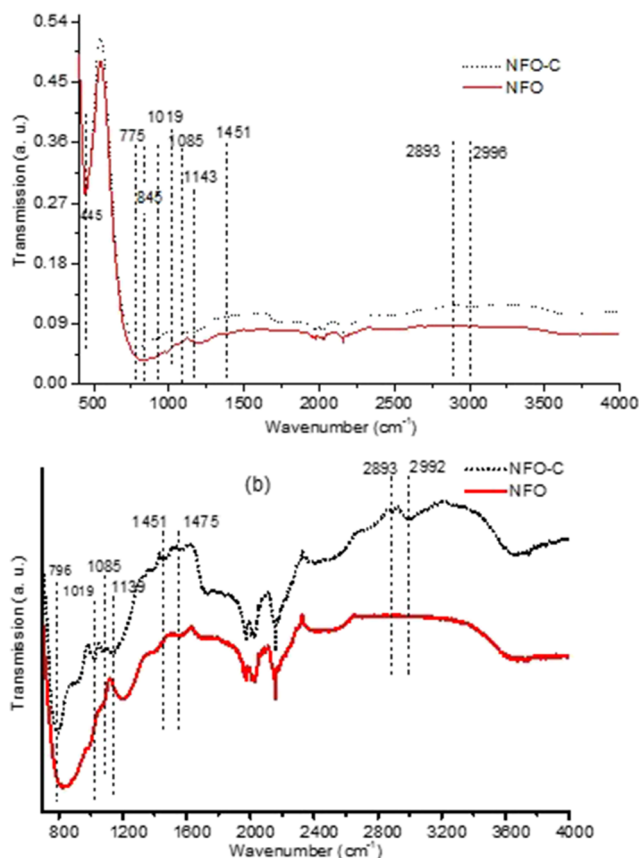
FIG. 5. FTIR spectra of NFO and NFO–C at full-range (a) and short-range (b) wavenumbers.

that of NFO. This shift indicates the coordination of the metal ions to ligands present in CDs.[41,42]

In-depth studies of the peaks present in the wavelength range 800–4000 cm^{-1} [Fig. 5(b)] reveal additional peaks present only in the spectra of NFO-C. The transmittance peaks at 1575 cm^{-1} and 1451 cm^{-1} associated with C=C and C–N bonds, respectively, were observable only in the spectra of CDs.[33] Peaks at 1085 cm^{-1} and 1139 cm^{-1} associated with C–OH vibrations were also observed in the spectra of CDs.[43] Two peaks appearing at 2893 cm^{-1} and 2992 cm^{-1} ascribed to the vibrations of CH molecules were present in the spectra of CDs.[44] The presence of these additional peaks in the spectra of NFO-C confirms the successful coordination of CDs to NFO. Furthermore, the CDs contained nitrogen functionalities.

Optical properties

Light absorption properties of NFO and NFO-C were investigated by using UV-VIS-NIR diffuse reflectance spectroscopy [Fig. 6(a)]. The absorbance spectra of NFO exhibited a distinct increase in absorption in the UV-VIS range at ~200 nm to 700 nm and 730 nm to 800 nm similar to those reported for other NFOs.[45] In addition to these, NFO showed an absorption in the NIR region at ~900 nm to 1400 nm. From the spectra of NFO-C, absorptions are evident in the UV-VIS region at ~200 nm to 700 nm and 730 nm to 800 nm similar to those of NFO. However, no absorption was observable in the NIR region between ~900 nm to 1400 nm. Additionally, the absorption maxima at ~745 nm were diminished in NFO-C compared with NFO [Fig. 6(a)]. Thus, it is evident that conjugation of CDs to NFO significantly alters the optical properties of NFO by completely quenching the NIR absorption and significantly minimizing the absorptions at ~745 nm. In a similar manner, Subramanian *et al.* reported a quenching in UV-VIS absorption of the TiO$_2$–Au composite at ~675 nm with increasing Au concentration.[46] In their studies, they attributed this quenching effect to the transfer of accumulated electron from TiO$_2$ to Au nanoparticles acting as electron acceptors. Likewise, the observed quenching of visible (~745 nm) and NIR absorption in NFO-C can be ascribed
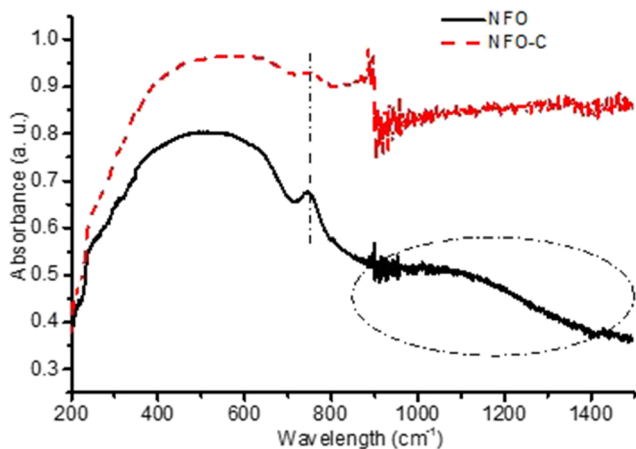
to metal–ligand center interactions leading to transfer of accumulated electrons from the HOMO of NFO to the LUMO of CDs. Such electron transfer from NFO to CDs is facilitated by π- or σ-bonds formed between the broken bonds in NFO nanoparticles and the ligands present in CDs as observed from the FTIR spectra of NFO-C [Fig. 5(b)].[47] Thus, CDs acting as electron reservoirs accepted accumulated electrons from NFO, consequently altering its optical properties. A further study of the electron transfer processes in both samples was henceforth conducted using impedance spectroscopy and laser flash photolysis.

The optical bandgaps for the allowed direct transitions of NFO and NFO-C were determined using DASF equation given by

$$\underbrace{\frac{\left(d\left\{In\left[\frac{f(R)}{\lambda}\right]\right\}\right)}{d\left(\frac{1}{\lambda}\right)}}_{A} = \frac{m}{\left(\frac{1}{\lambda} - \frac{1}{\lambda_g}\right)},$$

where R is the reflectance, λ is the wavelength of reflectance, λ_g is the wavelength of the allowed bandgap energy, and m is an index.[7,48] Figure 7 shows the DASF plot of the energy $[1/\lambda(eV)]$ against the factor A for NFO and NFO-C. The direct bandgaps for both samples were determined from the peak maxima of the allowed transition.
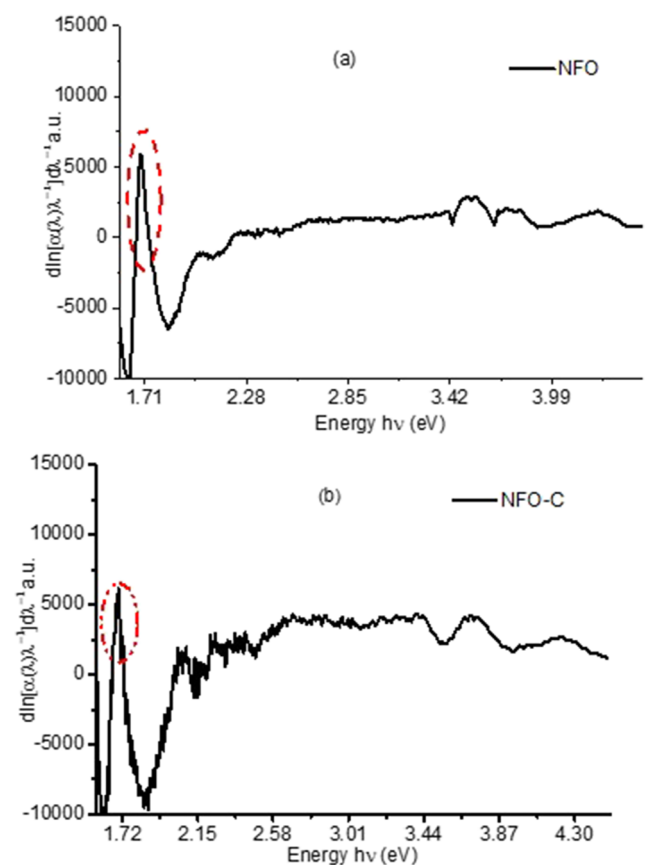

FIG. 7. DASF plot depicting the optical bandgap of NFO (a) and NFO-C (b).

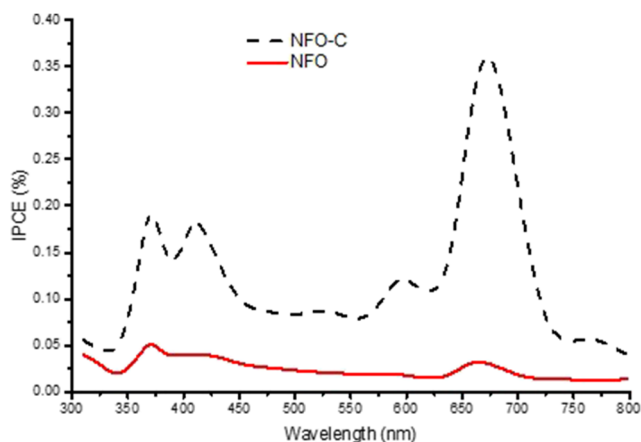**FIG. 6**. UV-VIS-NIR diffuse reflectance spectra of NFO and NFO-C.

FIG. 8. IPCE spectra of NFO and NFO–C.

Based on these plots, the direct bandgap for both NFO and NFO–C was determined to be 1.7 eV, which is similar to that reported for other ferrites.[49] Thus, conjugation of CDs to NFO did not alter the bandgap energy of NFO.

Photoelectrochemical and photochemical analysis

The IPCE spectra of NFO and NFO–C obtained at 0.4 V vs Ag/AgCl electrode (3M KCl) and at varying wavelengths are presented in Fig. 8. Both samples displayed four distinct IPCE thresholds at approximately 370 nm, 415 nm, 595 nm, and 675 nm with values ranging from 0.1% to 0.36%. The highest IPCE threshold value of 0.36% was observed at 675 nm with NFO–C, this wavelength is close to that reported for the highest IPCE threshold of zinc ferrite nanoparticles.[50]

Interestingly, a comparison of the UV-VIS-NIR spectra of both samples (Fig. 6), revealed a significant difference between the absorption of NFO and NFO–C in the range of 650–1400 nm. It appears that the effect of electronic interactions between CDs and NFO is the strongest within this wavelength range. As evidenced from the UV-VIS-NIR spectra (Fig. 6), upon irradiation of NFO–C with the full spectrum of light, electrons are transferred from the HOMO of NFO to the LUMO of CDs. This improves electron–hole separation in NFO consequently availing more holes for the

oxidation of water which translates into an enhanced IPCE performance in NFO–C,[51] thus indicating that CDs are capable of mediating the electron transfer process in NFO. In general, higher IPCE values are observable with NFO–C compared with NFO for the entire scan range. Nonetheless, the IPCE performance of both samples is lower than that reported for hematite, accounting for their lower photocatalytic activity.[52]

To correlate the enhanced IPCE performance of NFO–C to improved charge-carrier dynamics, electrochemical impedance spectroscopy (EIS) was conducted. EIS is a convenient technique for investigating the electrical properties, charge-carrier separation, and interfacial charge transfer processes in materials.[53] The complex impedance plots of various materials are usually semi-circles with a radius linearly correlating with the charge transfer impedance (resistance) of the material.[54] A comparison of the complex impedance spectra of NFO–C and NFO reveals a much lesser arc radius for NFO–C compared with that of NFO [Fig. 9(a)]. This indicates a reduced charge transfer resistance in NFO–C [Fig. 9(b)] resulting from improved electron–hole separation processes, faster interfacial charge transfer, and better conductivity.[55] Such an enhancement of charge-carrier separation and interfacial charge transfer in NFO–C may have resulted in the higher zeta potential and solution conductivity observed with this sample. The oxygen- and nitrogen-functionalized CDs acted as good electron reservoirs for NFO by accepting electrons from the conduction band of NFO. This elongated the lifetime of holes in the valence band of NFO, resulting in an enhanced interfacial charge transfer in NFO–C.

Possibly, the transfer of electrons from the HOMO of NFO to the LUMO of CDs is facilitated by a favorable placement of the energy levels in CDs relative to that of NFO. The observed NIR peak quenching and diminishing of visible-light absorption at ~745 nm further supports the likelihood of such electron transfer processes. Hence, conjugating CDs to NFO improved the charge-carrier separation, conductivity, and wettability of NFO–C, resulting in improved IPCE performance and interfacial charge transfer.

In order to understand the origin of the enhanced charge-carrier separation in NFO–C, transient reflectance spectroscopy was conducted in a N_2 and N_2–MeOH atmosphere [Figs. 10(a) and 10(b)]. For these experiments, nitrogen provided an inert atmosphere while methanol acted as an h^+ scavenger. Figure 10(a) represents the transient reflectance spectra of NFO and NFO–C
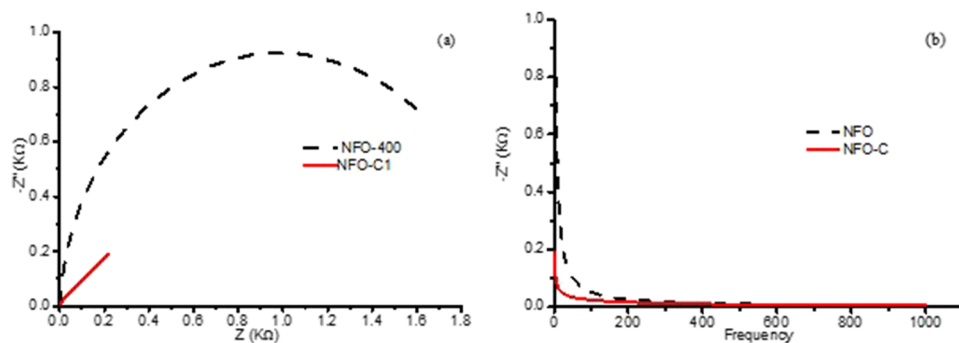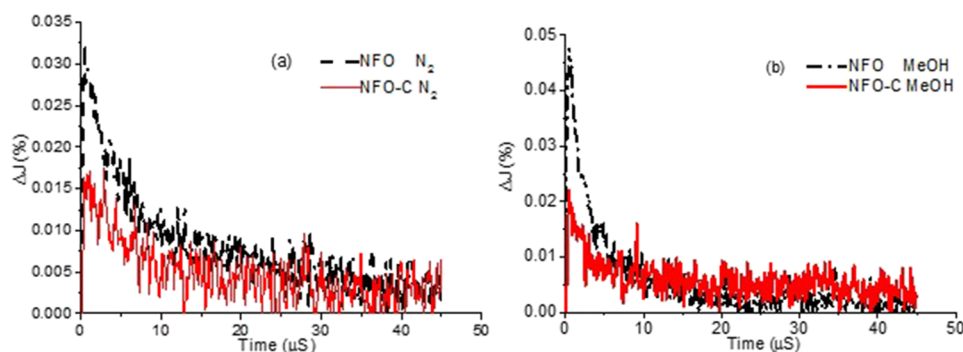

FIG. 9. Electrochemical impedance spectra (a) and variation of the resistance with frequency (b) of NFO and NFO–C.

FIG. 10. Transient absorbance of NFO and NFO–C in nitrogen (a) and methanol (b) at 550 nm^{-1} resulting from a 1.5 mJ/cm^2 laser pulse of 355 nm.

measured in an inert atmosphere, where the main source of charge-carrier decay is presumably recombination and/or transfer to ligands. From these figures, a lower initial quantity of charge carrier is observable in NFO–C compared with NFO. This is associated with the transfer of electrons from the conduction band of NFO to vacant π^*-orbitals in CDs acting as electron acceptors and reservoirs.[56] Such electron transfer processes are facilitated by the strong electronic interactions present between NFO and CDs as was observed from FTIR and UV-VIS-NIR investigations.[28] Consequently, CDs act as both electron acceptors and reservoirs, resulting in an improved charge separation and IPCE performance in NFO–C, which in turn can enhance the photocatalytic activity of this sample.

For both samples, two distinct absorption peaks are observable at 550 nm^{-1} and 600 nm^{-1} in an inert atmosphere, with the latter being more prominent than the former [Figs. 11(a) and 11(b)]. To distinguish between absorption peaks of trapped holes and electrons, transient reflectance spectra were recorded in methanol [Fig. 10(b)].[25] Since methanol is an h$^+$ scavenger, it reacts with the generated h$^+$, resulting in a decrease in the h$^+$ absorption peak and an increase in the e$^-$ absorption peak owing to accumulation of e$^-$ in the sample.[25]

A comparison of the absorption peak at 550 nm^{-1} in a N$_2$–MeOH and N$_2$ environment reveals a slight increase in absorption for NFO and an almost constant absorption for NFO–C [Figs. 12(a) and 12(b)]. This slight increase in absorption noted
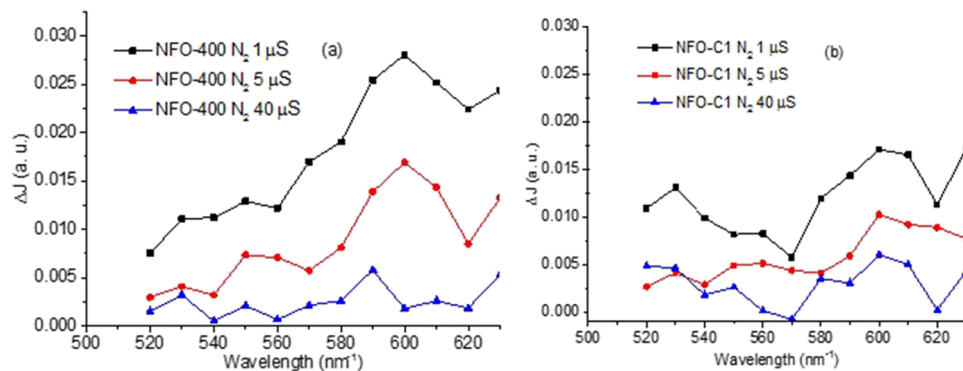
FIG. 11. Transient absorption spectra of NFO (a) and NFO–C (b) at 1, 5, and 40 μS in N$_2$.
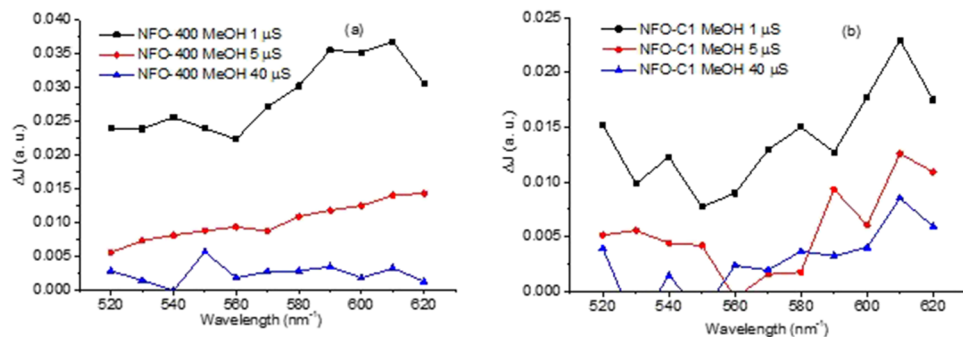
FIG. 12. Transient absorption spectra of NFO (a) and NFO–C (b) at 1, 5, and 40 μS in N$_2$–MeOH.

with NFO is attributed to a slow-paced accumulation of electrons upon consumption of holes by methanol in this sample. A similar accumulation is not evidenced in NFO–C since the electrons do not accumulate in NFO but are instead transferred to CDs. This transfer of electrons from NFO to CDs accounts for the improved hole transfer processes as evidenced by the enhanced IPCE performance of NFO–C over NFO. Compared to nitrogen, the absorption at 600 nm^{-1} in methanol significantly decreases after 40 μS for both samples (Figs. 11 and 12). Since the signal at 550 nm^{-1} increases or remains constant while the signal at 600 nm^{-1} decreases, we ascribe the former absorption peak to trapped electrons and the later to trapped holes in NFO. It is important to note that the signal at 600 nm^{-1} does not completely disappear even after 40 μS implying a very slow reaction between methanol and the generated holes in NFOs.

Photocatalytic oxidation of methanol to formaldehyde was employed as a model reaction to evaluate the influence of CDs on the photochemical properties of NFO.[57] UV-VIS analysis of aliquots of the catalysts suspended in methanol solution, sampled within 2-h of a dark reaction showed absorption peaks ranging from 350 nm to 500 nm. These peaks exhibited a peak maximum at ~412 nm, which is attributable to absorptions of formaldehyde or chromophores present on the surface of the catalysts. To probe the origin of this peak, control methanol oxidation reactions over NFO and NFO–C were conducted under argon atmosphere and visible light ($\lambda < 450$ nm). The absorption spectra of the methanol suspension sampled during 2 h of illumination exhibits no increment in the broad peak (350–500 nm) having a maximum at ~412 nm (see the supplementary material, S3). Hence, this peak is attributable to the absorption of chromophores present on the surface of the nanoparticles and not to formaldehyde formation. Consequently, the observed UV-VIS absorption peak of the methanol solution after the dark reaction is ascribable to the absorption of chromophores on the surface of the nanoparticles.

The constant intensity of this absorption peak with time indicates that the carbon dots do not leach from the surface of NFO–C during the photocatalytic reaction. Upon irradiating the methanol solution with visible light ($\lambda < 450$ nm and 660 nm), the quantity of formaldehyde detected over NFO–C steadily increases with time (Fig. 13 and Table III). On the contrary, the amount of formaldehyde produced over NFO reduces after 1.5 h of the reaction. Raman spectroscopic analysis of NFO and NFO–C after the photocatalytic reaction exhibit no phase changes in the catalysts after the reaction [see the supplementary material, S4 (a)]. Likewise, XRD analysis of NFO after the photocatalytic oxidation reaction reveals that no phase transformation occurred in the material during irradiation [see the supplementary material, S4 (b)]. Therefore, the steady increase of formaldehyde quantities with time over NFO–C alone implies that NFO–C does not undergo photocatalytic poisoning while NFO does, thus deterring its activity after 1.5 h.

No increase in intensity in the absorption peak maximum at ~412 nm is observable from the UV-VIS spectra of aliquots of a solution of pristine CDs and methanol samples within 2 h of irradiation (see the supplementary material, S3). Therefore, it is plausible that the slight increase in photocatalytic activity observed over NFO–C arises from charge separation enhancement in this sample. Based on
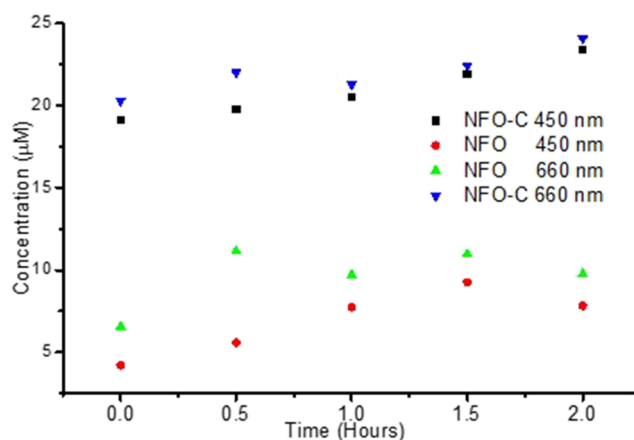

FIG. 13. Photocatalytic oxidation of MeOH solution over NFO and NFO—C under illumination.

the observed photocatalytic trends (Fig. 13), it is also evident that CDs enhance the photo-stability of NFO, which in turn enhances its photocatalytic activity, albeit to a small extent. The nanoparticle size and surface area of NFO (11.1 nm and 42 m^2 g^{-1}, respectively) did not significantly differ from that of NFO–C (11.3 nm and 39 m^2 g^{-1}, respectively). Therefore, the improved photocatalytic activity of NFO–C is accredited to its enhanced optical and photochemical properties owing to conjugation with CDs.

In view of the altered NIR and visible-light absorption, enhanced charge-carrier separation, and improved photocatalytic activity of NFO–C over NFO, we propose that the modification of NFO with CDs occur as follows: (1) During the synthesis of NFO–C, CDs having vacant π^*-orbitals and energy levels comparable to that NFO are coordinated to broken bonds in NFO nanoparticles. (2) Since the CDs possess low-lying empty π^*-orbitals, they act as effective electron acceptors and reservoirs, facilitating metal-to-ligand electron transfers (Fig. 14), thus enhancing charge-carrier separation. (3) The extended lifetime of holes in the valence band of NFO–C increases the quantity of methanol oxidized to formaldehyde (Fig. 13). The mechanism of methanol oxidation over NFO and NFO–C is thought to be similar to that extensively reported for methanol oxidation over TiO$_2$ and is presented as follows:[57,58]
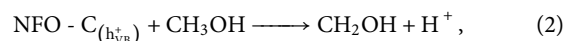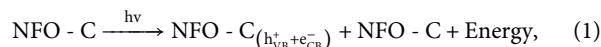
$$\text{NFO - C} \xrightarrow{h\nu} \text{NFO - C}_{(h^+_{VB} + e^-_{CB})} + \text{NFO - C} + \text{Energy}, \quad (1)$$

$$\text{NFO - C}_{(h^+_{VB})} + \text{CH}_3\text{OH} \longrightarrow \text{CH}_2\text{OH} + \text{H}^+, \quad (2)$$
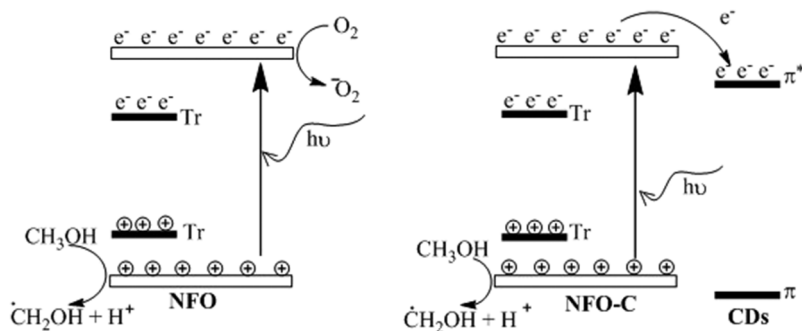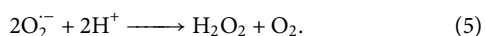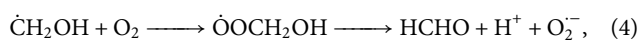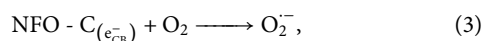
TABLE III. A summary of the photocatalytic activity of NFO and NFO–C after 2 h of illumination.

Irradiation wavelength (nm)	NFO Concentration (MM)	NFO–C Concentration (MM)
450	8	23
660	10	24

FIG. 14. Schematic representation of the proposed methanol photolysis mechanism over NFO and NFO–C; ∗Tr represents trap states.

$$NFO\text{-}C_{(e_{CB}^-)} + O_2 \longrightarrow O_2^{\cdot-}, \quad (3)$$

$$\dot{C}H_2OH + O_2 \longrightarrow \dot{O}OCH_2OH \longrightarrow HCHO + H^+ + O_2^{\cdot-}, \quad (4)$$

$$2O_2^{\cdot-} + 2H^+ \longrightarrow H_2O_2 + O_2. \quad (5)$$

CONCLUSION

Herein, we report for the first time the successful synthesis of the CDs/NiFe$_2$O$_4$ composite using ethylenediaminetetraacetic acid, tetraethylenepentamine, and citric acid via a simple two-step solvothermal approach. The synthetic strategy utilized tetraethylenepentamine as a source of primary and secondary amines that acylate to carbonyl groups present in ethylenediaminetetraacetic acid and citric acid, resulting in polyaromantic ring formation. The successful attachment of CDs to nickel ferrite was confirmed by elemental analysis and FTIR spectroscopy, which exhibited the presence of 0.18% carbon and CDs transmittance peaks, respectively, only for the CDs/NiFe$_2$O$_4$ composite.

Coordination of CDs to NFO does not alter the structure, morphology, and phase purity of pristine nickel ferrite as evidenced from TEM, SEM, XRD, and Raman spectroscopic studies. Analysis of the Raman modes corresponding to tetrahedral and octahedral vibrational modes indicates a higher degree of inversion for NFO–C compared with NFO.

Of great interest is the effect of conjugating CDs to NFO on the optical and photochemical properties of NFO. A total quenching of NIR absorbance and a decrease in visible-light absorbance at ~745 nm were observed from the UV-VIS-NIR spectra of NFO–C compared to that of NFO. Since no significant change in the optical bandgap was present between the two samples, the altered optical properties were attributed to metal-to-ligand electron transfer in NFO–C. An almost 12-fold increment in IPCE threshold, reduced impedance to charge-carrier transfer, and enhanced electron–hole separation were achieved with NFO–C compared with NFO. These observations all point toward CDs being good electron acceptors and reservoirs for NFO. Based on these observations, we have proposed a model for the energy level interactions between CDs and NFO. The enhanced photochemical and optical properties of NFO–C improved its photo-stability compared with pristine NFO as NFO–C did not undergo catalytic poisoning while NFO was poisoned. In general, CDs were good electron mediators for NFO,

enhancing the photochemical properties and photocatalytic activity of NFO. The findings of this study contribute toward understanding CDs as electron mediators in nickel ferrite. Consequently, future studies on the utilization of CDs for the improvement of photochemical and electrical properties of other spinel ferrites are a worthwhile venture.

SUPPLEMENTARY MATERIAL

See the supplementary material for DLS particle size analysis, Rietveld refinements of the XRD diffractograms of NFO and NFO–C, photocatalytic oxidation of MeOH solution over NFO and NFO–C under an argon atmosphere and CDs under an oxygen atmosphere, Raman spectra of NFO and NFO–C before and after photocatalytic oxidation of methanol, and XRD diffractograms of NFO before and after photocatalytic oxidation of methanol.

REFERENCES

[1] Z. Wang, C. Li, and K. Domen, Chem. Soc. Rev. **48**, 2109 (2018).

[2] F. F. Wang, Q. Li, and D. S. Xu, Adv. Energy Mater. **7**, 1700124 (2017).

[3] S. Chen, T. Takata, and K. Domen, Nat. Rev. Mater. **2**, 17050 (2017).

[4] B. De and N. Karak, J. Mater. Chem. A **5**, 1826 (2017).

[5] D. Taffa, A. C. U. Dillert, T. B. Katharina, C. L. Bauerfeind, T. Bredow, and D. W. Bahnemann, J. Photonics Energy **7**, 012009 (2012).

[6] S. Chandrasekaran, C. Bowen, P. Zhang, Z. Li, Q. Yuan, X. Ren, and L. Deng, J. Mater. Chem. A **6**, 11078 (2018).

[7] L. I. Granone, A. C. Ulpe, L. Robben, S. Klimke, M. Jahns, F. Renz, T. M. Gesing, T. Bredow, R. Dillert, and D. W. Bahnemann, Phys. Chem. Chem. Phys. **20**, 28267 (2018).

[8] A. Arimi, L. Megatif, L. I. Granone, R. Dillert, and D. W. Bahnemann, J. Photochem. Photobiol., A **366**, 118 (2018).

[9] N. Guijarro, P. Bornoz, M. Prévot, X. Yu, X. Zhu, M. Johnson, X. Jeanbourquin, F. Le Formal, and K. Sivula, Sustainable Energy Fuels **2**, 103 (2018).

[10] P. Iranmanesh, S. Saeednia, M. Mehran, and S. R. Dafeh, J. Magn. Magn. Mater. **425**, 31 (2017).

[11] P. Iranmanesh, S. T. Yazdi, M. Mehran, and S. Saeednia, J. Magn. Magn. Mater. **449**, 172 (2018).

[12] Z. Ž. Lazarević, Č. Jovalekić, A. Milutinović, D. Sekulić, V. N. Ivanovski, A. Rečnik, B. Cekić, and N. Ž. Romčević, J. Appl. Phys. **113**, 187221 (2013).

[13] L. I. Granone, R. Dillert, P. Heitjans, and D. W. Bahnemann, ChemistrySelect **4**, 1232 (2019).

[14] R. Dillert, D. H. Taffa, M. Wark, T. Bredow, and D. W. Bahnemann, APL Mater. **3**, 104001 (2015).

[15] N. C. T. Martins, J. Ângelo, A. V. Girão, T. Trindade, L. Andrade, and A. Mendes, Appl. Catal., B **193**, 67 (2016).

[16] X. Xu, R. Ray, Y. Gu, H. J. Ploehn, L. Gearheart, K. Raker, and W. A. Scrivens, J. Am. Chem. Soc. **126**, 12736 (2004).

[17] W. Liu, C. Li, Y. Ren, X. Sun, W. Pan, Y. Li, J. Wang, and W. Wang, J. Mater. Chem. B **4**, 5772 (2016).

[18] M. L. Liu, B. Bin Chen, C. M. Li, and C. Z. Huang, Green Chem. **21**, 449 (2019).

[19] H. X. Wang, J. Xiao, Z. Yang, H. Tang, Z. T. Zhu, M. Zhao, Y. Liu, C. Zhang, and H. L. Zhang, J. Mater. Chem. A **3**, 11287 (2015).

[20] A. Datta, S. Kapri, and S. Bhattacharyya, J. Mater. Chem. A **4**, 14614 (2016).

[21] M. K. Barman, B. Jana, S. Bhattacharyya, and A. Patra, J. Phys. Chem. C **118**, 20034 (2014).

[22] J. Wang, F. Ren, R. Yi, A. Yan, G. Qiu, and X. Liu, J. Alloys Compd. **479**, 791 (2009).

[23] J. Wang, W. Zhang, X. Yue, Q. Yang, F. Liu, Y. Wang, D. Zhang, Z. Li, and J. Wang, J. Mater. Chem. A **4**, 3893 (2016).

[24] S. Bhattacharyya, F. Ehrat, P. Urban, R. Teves, R. Wyrwich, M. Döblinger, J. Feldmann, A. S. Urban, and J. K. Stolarczyk, Nat. Commun. **8**, 1401 (2017).

[25] J. Schneider, K. Nikitin, M. Wark, D. W. Bahnemann, and R. Marschall, Phys. Chem. Chem. Phys. **18**, 10719 (2016).

[26] U. Kleeberg and W. Klinger, J. Pharmacol. Methods **8**, 19 (1982).

[27] B. M. Choudary, V. Bhaskar, M. L. Kantam, K. K. Rao, and K. V. Raghavan, Catal. Lett. **74**, 207 (2001).

[28] R. Wang, K. Q. Lu, Z. R. Tang, and Y. J. Xu, J. Mater. Chem. A **5**, 3717 (2017).

[29] S. Talukdar, R. Rakshit, A. Krämer, F. A. Müller, and K. Mandal, RSC Adv. **8**, 38 (2018).

[30] M. Kiani, J. Zhang, J. Fan, H. Yang, G. Wang, J. Chen, and R. Wang, Mater. Express **7**, 261 (2017).

[31] P. Sivakumar, R. Ramesh, A. Ramanand, S. Ponnusamy, and C. Muthamizhchelvan, Mater. Res. Bull. **46**, 2204 (2011).

[32] K. N. Subramanyam, J. Phys. C: Solid State Phys. **4**, 2266 (1971).

[33] L. M. Ombaka, P. G. Ndungu, and V. O. Nyamori, RSC Adv. **5**, 109 (2015).

[34] P. R. Graves, C. Johnston, and J. J. Campaniello, Mater. Res. Bull. **23**, 1651 (1988).

[35] Z. H. Zhou, J. M. Xue, J. Wang, H. S. O. Chan, T. Yu, and Z. X. Shen, J. Appl. Phys. **91**, 6015 (2002).

[36] J. Molina-Duarte, L. I. Espinosa-Vega, A. G. Rodríguez, and R. A. Guirado-López, Phys. Chem. Chem. Phys. **19**, 7215 (2017).

[37] M. Sertkol, Y. Köseoğlu, A. Baykal, H. Kavas, A. Bozkurt, and M. S. Toprak, J. Alloys Compd. **486**, 325 (2009).

[38] R. D. Waldron, Phys. Rev. **99**, 1727 (1955).

[39] A. A. Khan, M. Javed, A. R. Khan, Y. Iqbal, A. Majeed, S. Z. Hussain, and S. K. Durrani, Mater. Sci.-Pol. **35**, 58 (2017).

[40] M. Naushad, T. Ahamad, B. M. Al-Maswari, A. Abdullah Alqadami, and S. M. Alshehri, Chem. Eng. J. **330**, 1351 (2017).

[41] P. B. Koli, K. H. Kapadnis, and U. G. Deshpande, J. Nanostruct. Chem. **9**, 105 (2019).

[42] D. C. Bradley and M. H. Gitlitz, Nature **218**, 353 (1968).

[43] H. Liu, Z. Li, Y. Sun, X. Geng, Y. Hu, H. Meng, J. Ge, and L. Qu, Sci. Rep. **8**, 1086 (2018).

[44] S. Lin, C. Lin, M. He, R. Yuan, Y. Zhang, Y. Zhou, W. Xiang, and X. Liang, RSC Adv. **7**, 41552 (2017).

[45] K. Kombaiah, J. J. Vijaya, L. J. Kennedy, and K. Kaviyarasu, Mater. Chem. Phys. **221**, 11 (2019).

[46] V. Subramanian, E. E. Wolf, and P. V. Kamat, J. Am. Chem. Soc. **126**, 4943 (2004).

[47] D. F. Zhao, H. Yang, R. S. Li, J. Y. Ma, and W. J. Feng, Mater. Res. Innovations **18**, 519 (2014).

[48] D. Souri and Z. E. Tahan, Appl. Phys. B: Lasers Opt. **119**, 273 (2015).

[49] H. Zhang, Y. Zhou, S.-Q. Liu, Q.-Q. Gu, Z.-D. Meng, and L. Luo, Catalysts **8**, 405 (2018).

[50] A. A. Tahir and K. G. U. Wijayantha, J. Photochem. Photobiol., A **216**, 119 (2010).

[51] S. Kasi Matta, C. Zhang, A. P. O'Mullane, and A. Du, ChemPhysChem **19**, 3018 (2018).

[52] W. Cheng, J. He, Z. Sun, Y. Peng, T. Yao, Q. Liu, Y. Jiang, F. Hu, Z. Xie, B. He, and S. Wei, J. Phys. Chem. C **116**, 24060 (2012).

[53] D. Y. Jeon, H. Kim, M. W. Lee, S. J. Park, and G. T. Kim, APL Mater. **7**, 041118 (2019).

[54] I. Khan, N. Baig, and A. Qurashi, ACS Appl. Energy Mater. **2**, 607 (2019).

[55] X. Gao, X. Liu, Z. Zhu, X. Wang, and Z. Xie, Sci. Rep. **6**, 30543 (2016).

[56] J. Nie, A. O. T. Patrocinio, S. Hamid, F. Sieland, J. Sann, S. Xia, D. W. Bahnemann, and J. Schneider, Phys. Chem. Chem. Phys. **20**, 5264 (2018).

[57] M. Curti, A. Kirsch, L. I. Granone, F. Tarasi, G. López-Robledo, D. W. Bahnemann, M. M. Murshed, T. M. Gesing, and C. B. Mendive, ACS Catal. **8**, 8844 (2018).

[58] S. Goldstein, D. Behar, and J. Rabani, J. Phys. Chem. C **112**, 15134 (2008).